ACS NANO

www.acsnano.org

ARTICLE

Ultrafast Electronic Relaxation Dynamics of Atomically Thin MoS_2 Is Accelerated by Wrinkling

Ce Xu, Guoqing Zhou, Evgeny M. Alexeev, Alisson R. Cadore, Ioannis Paradisanos, Anna K. Ott, Giancarlo Soavi, Sefaattin Tongay, Giulio Cerullo, Andrea C. Ferrari,* Oleg V. Prezhdo,* and Zhi-Heng Loh*

Cite This: *ACS Nano* 2023, 17, 16682−16694

Read Online

ACCESS | Metrics & More | Article Recommendations | Supporting Information

ABSTRACT: **Strain engineering is an attractive approach for tuning the local optoelectronic properties of transition metal dichalcogenides (TMDs). While strain has been shown to affect the nanosecond carrier recombination dynamics of TMDs, its influence on the sub-picosecond electronic relaxation dynamics is still unexplored. Here, we employ a combination of time-resolved photoemission electron microscopy (TR-PEEM) and nonadiabatic *ab initio* molecular dynamics (NAMD) to investigate the ultrafast dynamics of wrinkled multilayer (ML) MoS_2 comprising 17 layers. Following 2.41 eV photoexcitation, electronic relaxation at the Γ valley occurs with a time constant of 97 ± 2 fs for wrinkled ML-MoS_2 and 120 ± 2 fs for flat ML-MoS_2. NAMD shows that wrinkling permits larger amplitude motions of MoS_2 layers, relaxes electron−phonon coupling selection rules, perturbs chemical bonding, and increases the electronic density of states. As a result, the nonadiabatic coupling grows and electronic relaxation becomes faster compared to flat ML-MoS_2. Our study suggests that the sub-picosecond electronic relaxation dynamics of TMDs is amenable to strain engineering and that applications which require long-lived hot carriers, such as hot-electron-driven light harvesting and photocatalysis, should employ wrinkle-free TMDs.**

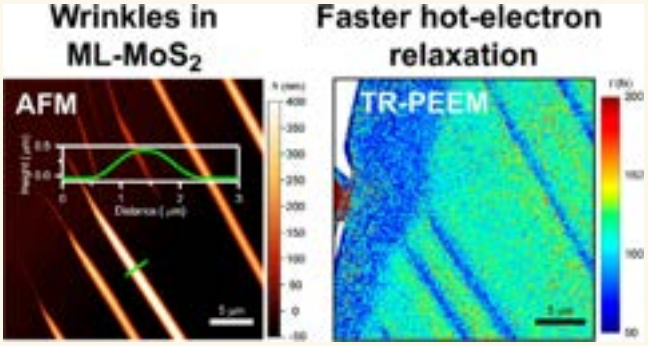

KEYWORDS: *transition metal dichalcogenides, ultrafast carrier dynamics, strain engineering, electron−phonon scattering, time-resolved photoemission electron microscopy, nonadiabatic ab initio molecular dynamics*

Transition metal dichalcogenides (TMDs) are a class of layered materials (LMs) with a range of electronic[1−3] and optoelectronic[2,4,5] properties. Semiconducting TMDs undergo an indirect-to-direct bandgap transition when their thickness is reduced down to a single layer (1L).[6,7] 1L-TMDs demonstrate high carrier mobilities (~10^1−10^3 $cm^2 \cdot V^{-1} \cdot s^{-1}$),[8,9] valley selectivity in photoexcitation,[10,11] and large nonlinear optical response [$\chi^{(2)} \sim 10^{-12}$−10^{-11} $m \cdot V^{-1}$, $\chi^{(3)} \sim 10^{-19}$−10^{-17} $m^2 \cdot V^{-2}$],[12−14] and their optical properties are dominated by excitonic resonances.[15−18] These properties, along with the ability to fabricate wafer-scale TMD thin films,[1−5] pave the way for a variety of applications in photodetectors,[19−22] light-emitting diodes,[23−25] transistors,[21] and modulators.[26]

The versatility of TMDs and their range of applications[2] can be further extended by tuning their electronic band structure,[27] e.g., by changing the composition.[3] Various synthesis procedures yield a family of TMDs comprising members with different chemical compositions,[5,28] each exhibiting a unique bandgap and band offsets relative to one another. The properties can be further tuned by chemical doping, e.g., by introducing intercalating metals or molecules,[29] or by substitutional doping with transition metals,[30] or by alloying.[31,32] For a fixed chemical composition, the band structure can be varied by applying electric fields,[33,34] pressure,[35,36] or strain.[37−40]

The mechanical properties of TMDs[41,42]—large Young's modulus (~0.4 TPa),[41,43] high breaking strength (~20

Received: March 31, 2023
Accepted: July 28, 2023
Published: August 15, 2023

https://doi.org/10.1021/acsnano.3c02917
ACS Nano 2023, 17, 16682−16694

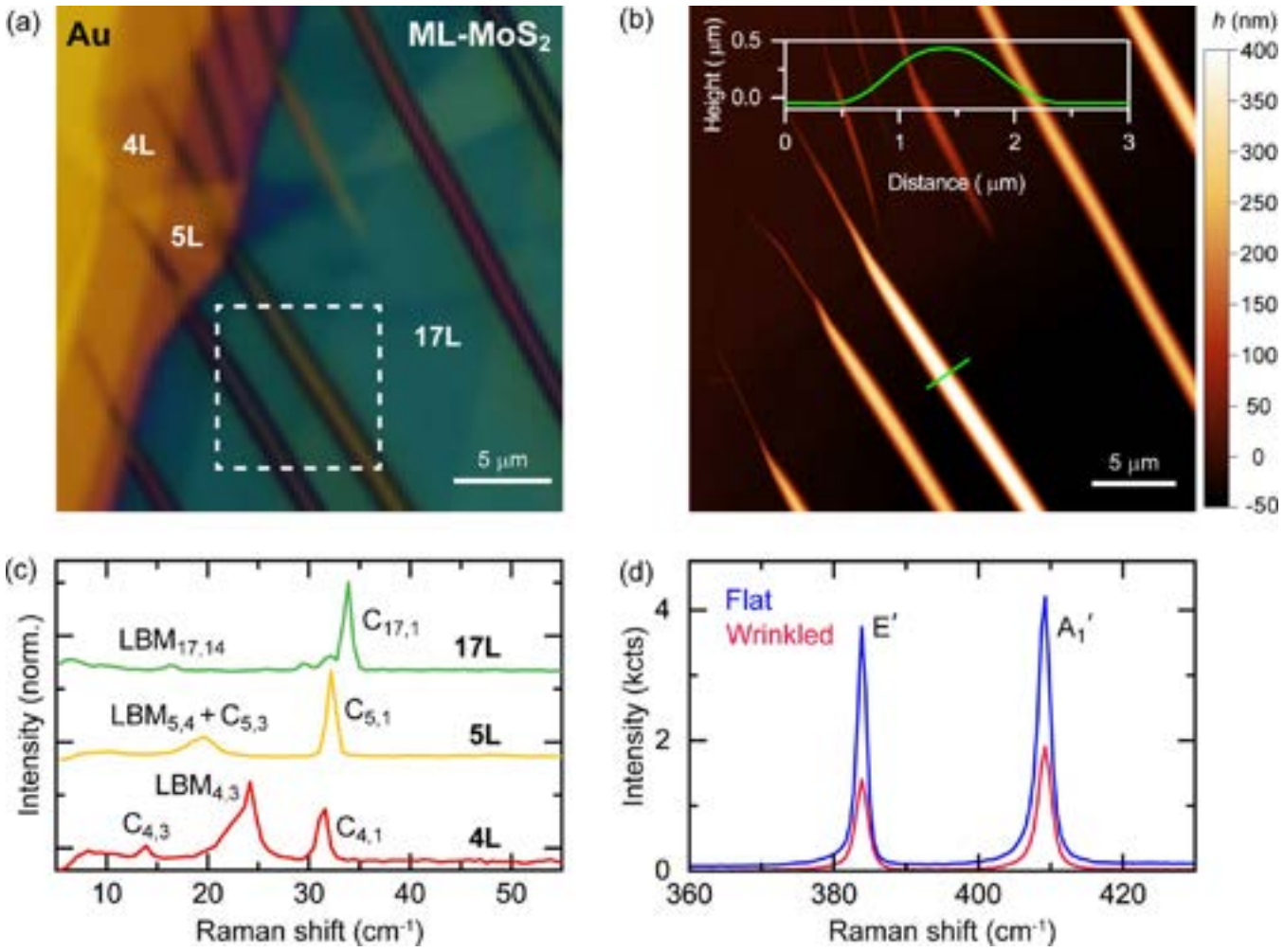

Figure 1. (a) Optical and (b) AFM images of the wrinkled ML-MoS_2 flake. The Au substrate and the layer numbers of the MoS_2 regions of the sample are labeled in (a). The inset in (b) shows the height profile across a wrinkle along the green line. (c) Normalized ultralow frequency Raman spectra showing the shear (C) and layer breathing (LBM) mode peaks for ML-MoS_2 with N = 4, 5, 17, collected with a 514 nm laser. (d) Raman spectra of the flat and wrinkled 17L-MoS_2 regions.

GPa),[41,43] and elasticity[44,45]—make them amenable to strain engineering.[39,46,47] This approach to tuning the band structure[48−50] has been exploited, e.g., to drive a semiconductor-to-metal transition in TMDs,[51] to realize a superlattice of artificial atoms in strain-textured MoS_2,[52] and to improve the performance of TMDs in optoelectronic devices.[53−55] While the effect of strain on bandgaps[56] and steady-state optoelectronic properties[53−55] of TMDs has been extensively investigated,[37−40,57] its influence on the nonequilibrium carrier dynamics of TMDs is still unexplored. Information on ultrafast carrier dynamics is needed to understand the carrier transport and optoelectronic characteristics of semiconductors.[58] *Ab initio* simulations of TMDs[59] and their heterostructures[60] reveal that strain affects the time scales for electronic dephasing,[59] carrier recombination,[59] and charge transfer.[60] Time-resolved photoluminescence (PL) studies of 1L-TMDs on flexible strained substrates revealed an increase in carrier recombination rate with strain in 1L-$MoSe_2$ and 1L-WSe_2,[61] whereas the carrier recombination dynamics of 1L-WS_2 was reported to be insensitive to strain,[61] attributed to weaker exciton−phonon coupling in S-based than Se-based TMDs.[61]

Here, we present an experimental−theoretical study of the ultrafast dynamics of wrinkled, multilayer (ML) MoS_2 comprising 17 layers. Micrometer-sized wrinkles of 0.5 μm height and 2 μm width result in localized strain. Time-resolved photoemission electron microscopy (TR-PEEM) combines the pump−probe technique with a PEEM microscope to simultaneously achieve high spatial (<80 nm) and temporal (<60 fs) resolution,[62,63] making it ideal for investigating the ultrafast dynamics of spatially heterogeneous samples.[64−69] We show that wrinkled ML-MoS_2 undergoes ∼1.2× faster electron cooling than flat ML-MoS_2. *Ab initio* molecular dynamics shows that wrinkling increases nonadiabatic coupling up to ∼1 eV above the ML-MoS_2 conduction band minimum (CBM), hence accelerating electronic relaxation.

RESULTS AND DISCUSSION

Figure 1a is an optical microscope image of a representative sample, containing regions with different numbers of layers (N). The wrinkles propagate through areas with different N and can be distinguished from flat ML-MoS_2 by their different color and optical contrast. Figure 1b is a topography map of the same region acquired by atomic force microscopy (AFM). The inset plots the cross-sectional height profile of the wrinkle

https://doi.org/10.1021/acsnano.3c02917
ACS Nano 2023, 17, 16682−16694

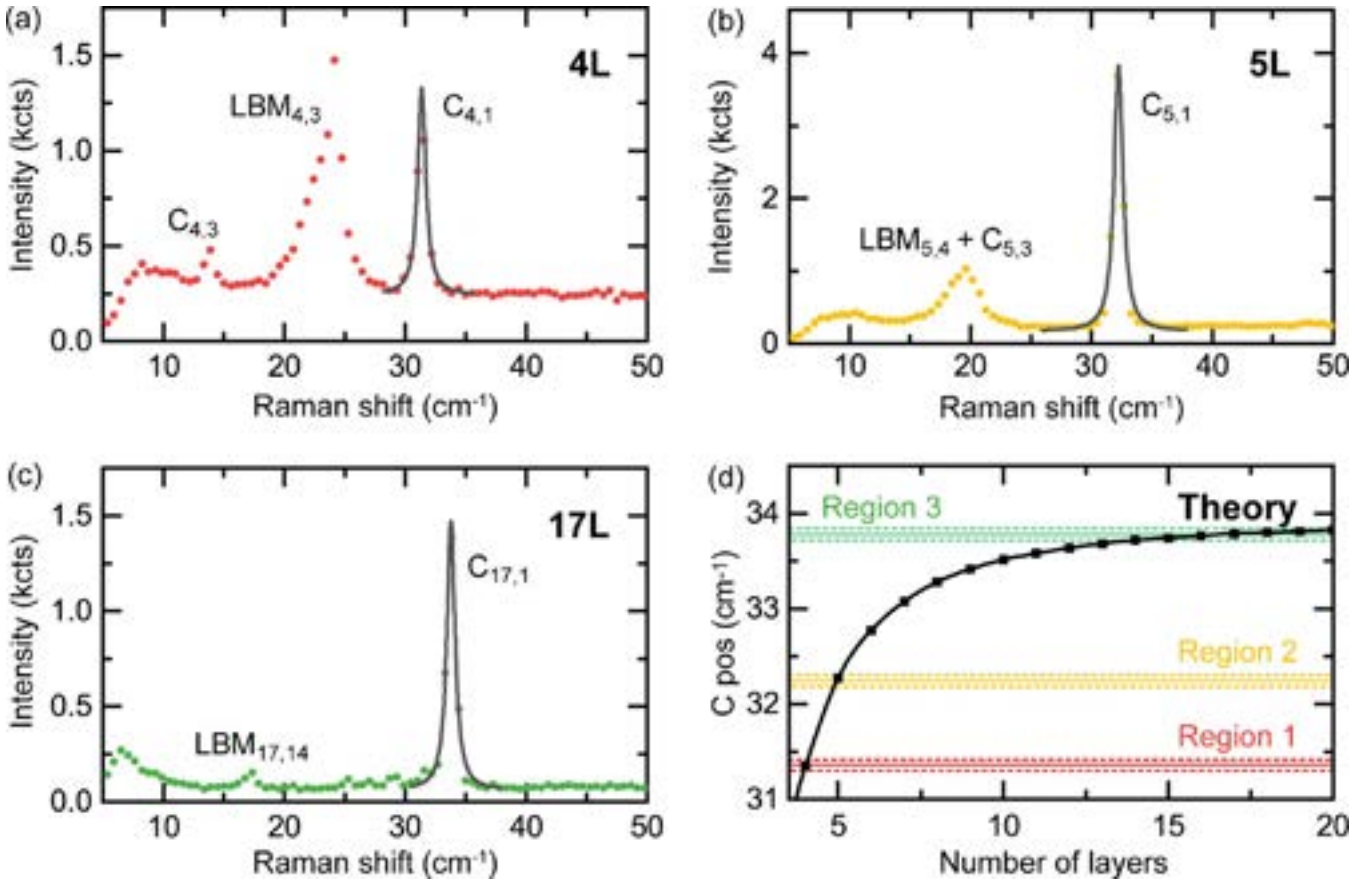

Figure 2. Ultralow frequency Raman spectra showing shear ($C_{N,N-j}$) and LBM ($LBM_{N,N-j}$) peaks in a MoS_2 flake with thicknesses of (a) 4L, (b) 5L, and (c) 17L, collected with a 514 nm laser. The solid lines are fits of $C_{N,1}$ to a Lorentzian line shape to determine the peak position, Pos($C_{N,1}$). (d) Plot of Pos($C_{N,1}$) vs number of layers. The black curve is the plot of eq 1 based on Pos(C_∞) = 33.93 cm^{-1}. The colored solid lines are Pos($C_{N,1}$) for the three ML-MoS_2 regions with dashed lines indicating the total fitting error.

along the direction shown by the green line in Figure 1b. Statistical analysis of three height profiles along a 5 μm length yields a mean (standard deviation) of 2.07 μm (0.02 μm) and 0.50 μm (0.01 μm) for width and height, respectively (see Supporting Information).

Raman spectroscopy is used to identify N and quantify strain. Figure 1c and 1d plot the respective low- (<50 cm^{-1}) and high-frequency (350−450 cm^{-1}) Raman spectra of different regions of the MoS_2 flake. Shear (C) and layer breathing (LBM) modes correspond to motion parallel and perpendicular to the layer plane, respectively.[70−72]

Figures 2a−c compare spectra recorded in three different regions. Spectral fitting yields Pos($C_{N,1}$) ~ 31.36 ± 0.06 cm^{-1}, 32.24 ± 0.06 cm^{-1}, and 33.78 ± 0.06 cm^{-1}. Figure 2d plots the change of Pos($C_{N,1}$) as a function of N, with Pos(C_∞) = 33.93 cm^{-1} for bulk MoS_2. Colored lines represent Pos($C_{N,1}$) in the three regions with associated fitting error indicated by dashed rectangles. This can be used to derive N as[71−73]

$$N = \frac{\pi}{2\cos^{-1}[\mathrm{Pos}(C_{N,1})/\mathrm{Pos}(C_\infty)]} \quad (1)$$

where Pos(C_∞) = 33.93 cm^{-1} is Pos($C_{N,1}$) in bulk MoS_2.

The spectrum recorded in the first region (red curve, Figure 1c) shows Pos($LBM_{4,3}$) = 24.24 ± 0.06 cm^{-1} and Pos($C_{N,1}$) = 31.36 ± 0.06 cm^{-1}, corresponding to N = 4. The second region (orange curve) has Pos($LBM_{5,4}$ + $C_{5,3}$) = 19.35 ± 0.06 cm^{-1} and Pos($C_{N,1}$) = 32.24 ± 0.06 cm^{-1}, giving N = 5. The third region (green) has Pos($LBM_{17,14}$) = 17.15 ± 0.06 cm^{-1} and Pos($C_{N,1}$) = 33.78 ± 0.06 cm^{-1}, giving N = 17 ± 3. Hereafter, we focus on the changes occurring in the N = 17 region.

Figure 1d compares the high-frequency (350−450 cm^{-1}) Raman spectra of flat and wrinkled 17L-MoS_2. The two peaks are the in-plane E' ~ 383.9 cm^{-1} and the out-of-plane A_1' ~ 409.1 cm^{-1} modes.[74] To accurately determine changes in Raman parameters in wrinkled 17L-MoS_2, we acquired maps in the area highlighted by the white square in Figure 1a. Maps of peak intensities and peak positions of the E' and A_1' modes are given in Figure 3

Wrinkled regions are identified in the peak intensity maps (Figures 3a,b), as the bending of MoS_2 layers leads to a ~70% reduction in the intensity of both E' and A_1'. Pos(E') in the wrinkled regions shows a red-shift compared to the surrounding flat areas (Figure 3c). Larger wrinkles located close to a diagonal show a stronger softening of E', with a red-shift of ≤0.18 cm^{-1}. A weaker red-shift is seen for the smaller wrinkle close to the bottom-right corner, ≤0.14 cm^{-1}. Pos(A_1') does not show a trend and is compatible with random variations in flat regions (Figure 3d). E' softens with tensile strain[75] by ~7.4 cm^{-1}/%.[76] A_1' is weakly coupled to strain,[76] but sensitive to doping,[77] softening with increasing electron density.[77] Thus, Raman microscopy is consistent with tensile strain ε < 0.03%.

To investigate the effect of wrinkles on the electronic relaxation dynamics, we carry out TR-PEEM measurements

https://doi.org/10.1021/acsnano.3c02917
ACS Nano 2023, 17, 16682−16694

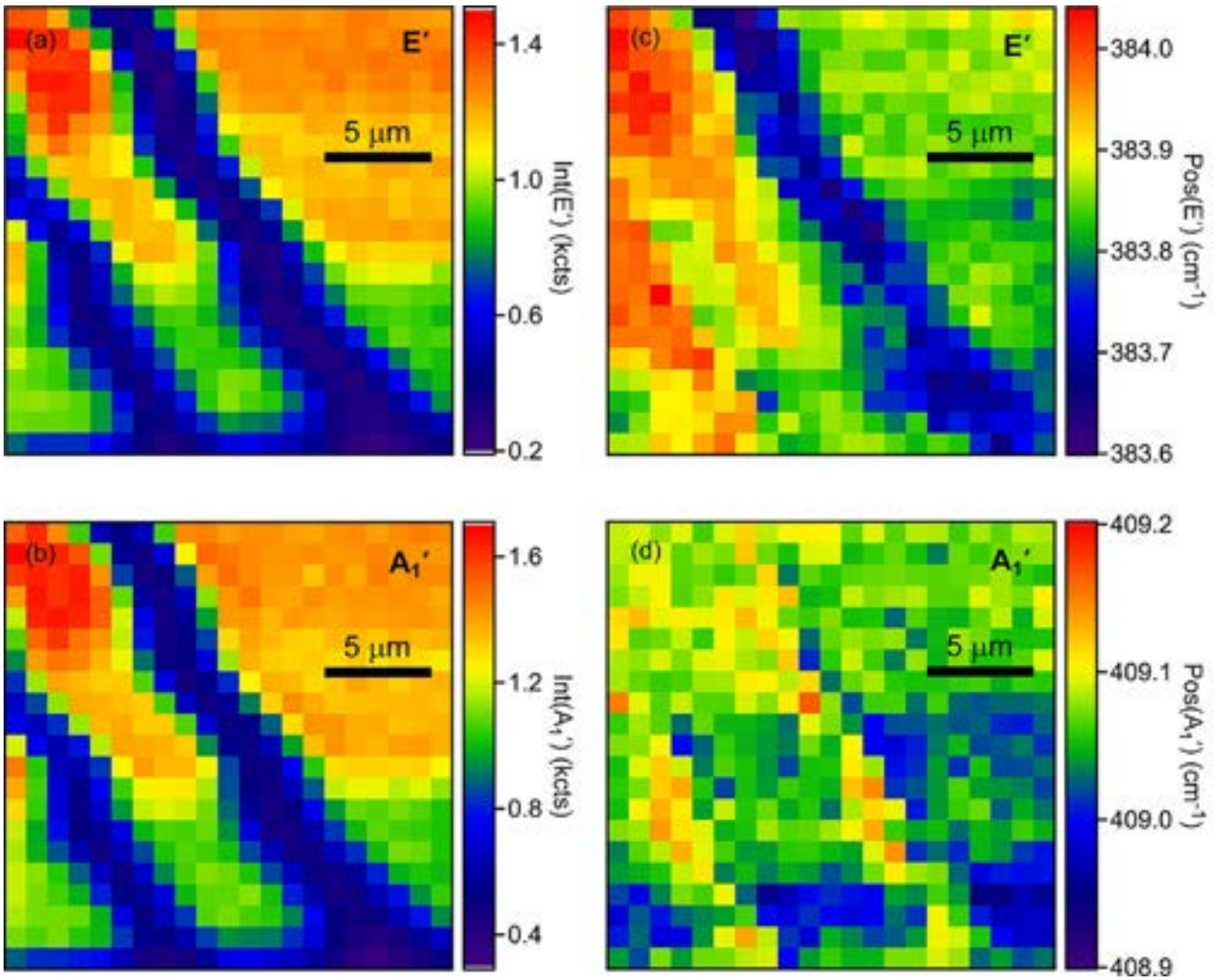

Figure 3. Intensity maps of (a) E' and (b) A_1' modes acquired at the position indicated by the white square in Figure 1a. Peak position maps of the (c) E' and (d) A_1' modes acquired in the same region.

with a 2.41 eV pump and 3.61 eV probe (see Supporting Information for details of the experimental setup). Electrons (e) in the valence band (VB) are excited to the conduction band (CB) by the 2.41 eV pump. After a variable time delay of −0.5 to +1.5 ps, a 3.61 eV probe pulse ejects these e, which are refocused by a column of electrostatic lenses onto an array detector to yield the PEEM image.[62,63] Power-dependent measurements reveal that the pump and probe interactions with the sample are both one-photon processes (Supporting Information). The lateral momentum conservation requirement in photoemission[78] confines the probe window for 3.61 eV probing to the vicinity of the Γ point of the CB (blue-shaded areas in Figure 4a, see Supporting Information). The ML-MoS_2 band structure[79] confirms that this region is readily accessed by 2.41 eV photoexcitation.

Accordingly, we infer that the observed ultrafast dynamics originates from electronic relaxation from the vicinity of the Γ point. Following photoexcitation, e can relax via a combination of intravalley and intervalley electron−phonon (e−ph) scattering[80−82] to reach the CBM prior to carrier recombination (Figure 4a). Figure 4b is a series of TR-PEEM images acquired at pump−probe time delays of 0, 40, 80, 120, 200, and 400 fs. The Au substrate exhibits the most intense PEEM signal.[68] 4L- and 5L-MoS_2 regions adjacent to it have higher count rates than the 17L region, most likely due to the nonmonotonic variation of the UV photoionization cross section with N.[83] Figure 4c plots the temporal evolution of the TR-PEEM signals, spatially integrated over wrinkled and flat regions (boxed regions in Figure 4b), chosen based on the uniform thickness over an extended area (~35 μm^2). The time traces can be fit to the instrumental response function convolved with a single-exponential decay, with time constants of 97 ± 2 fs for wrinkled and 120 ± 2 fs for flat ML-MoS_2. The decay of the PEEM signal tracks the electronic relaxation dynamics at Γ, as they undergo e−ph scattering[66,69] and leave the probe window to populate the lower-lying valleys in the CB (Figure 4a). We can rule out the possibility that e transfer to the underlying Au substrate contributes to the observed dynamics,[68] since the interaction with the substrate is expected to be stronger for flat MoS_2, in contrast with the faster decay of TR-PEEM observed for the wrinkled regions in Figure 4c.

To confirm that electronic relaxation rates are enhanced at wrinkles, we extract the time traces for each pixel of the TR-PEEM image and fit them to a single-exponential decay

https://doi.org/10.1021/acsnano.3c02917
ACS Nano 2023, 17, 16682−16694

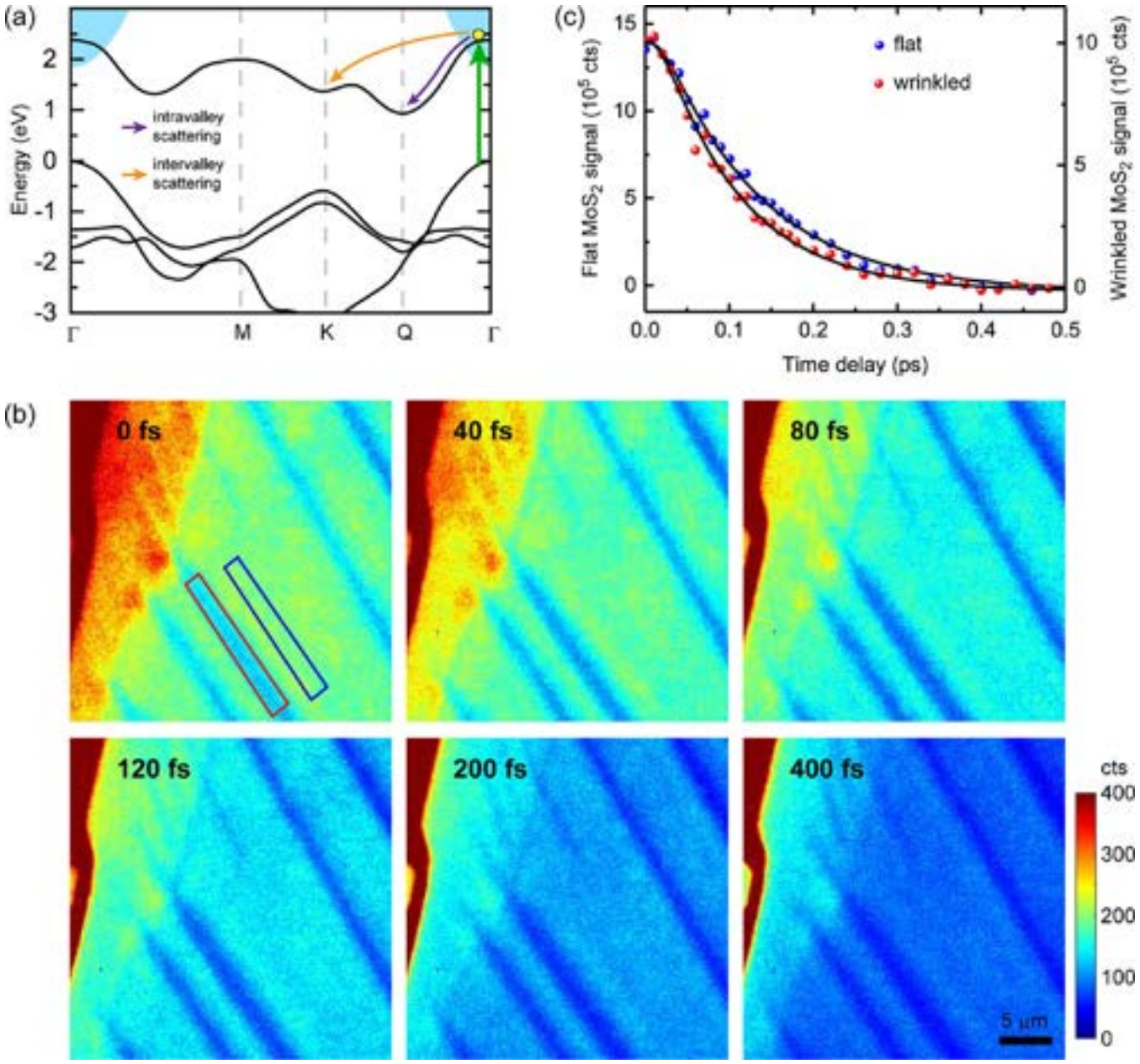

Figure 4. (a) Schematic of intravalley and intervalley scattering from Γ following excitation at 2.41 eV (green arrow). The blue-shaded areas represent the window for a 3.61 eV probe. Band structure from ref 79. (b) PEEM images of wrinkled ML-MoS_2 with a series of time delays. The PEEM signal is lower for wrinkled than for flat ML-MoS_2. (c) Time traces of wrinkled ML-MoS_2 (red box in b) and flat ML-MoS_2 (blue box in b), fitted by single-exponential decay, after time-zero convolved with the instrumental response function.

convolved with the 55 fs FWHM instrumental response function (cross-correlation of the temporal intensity profiles of the 2.41 and 3.61 eV pulses). The time constant at each pixel is used to create a lifetime map that reveals the spatial distribution of relaxation times (Figure 5a). Prominent blue stripes in the lifetime map, which encode regions with shorter relaxation times, coincide with the wrinkles. Figure 5b plots histograms of relaxation times on wrinkled and flat ML-MoS_2, extracted from the regions of interest defined in Figure 4b. These have a mean (standard deviation) of 89 (14 fs) and 114 fs (14 fs) for the wrinkled and flat regions, respectively (see Supporting Information for histograms of other wrinkles). The lifetime map and histograms both reveal faster electronic relaxation in the wrinkled region, in good agreement with the results obtained from the analysis of the spatially integrated time traces (Figure 4c). The slight deviation between the two sets of values arises from the fact that the lifetime obtained from the spatially integrated measurement represents an amplitude-weighted average time constant instead of a simple average.

To model the impact of wrinkles on carrier dynamics in ML-MoS_2, we build two periodic systems, representing flat and wrinkled bulk MoS_2 (B-MoS_2), shown in Figures 6a and 6b, respectively. The B-MoS_2 models are represented by rectangular simulation cells with 1 × 10 × 1 MoS_2 unit cells, replicated along the armchair direction and containing 120 atoms each. This is done to model an undulation mimicking the experiment, although on a nanometer rather than micrometer scale due to computational limitations. The length of the supercell for flat B-MoS_2 is 54.5 Å. Wrinkled B-MoS_2 is

https://doi.org/10.1021/acsnano.3c02917
ACS Nano 2023, 17, 16682−16694

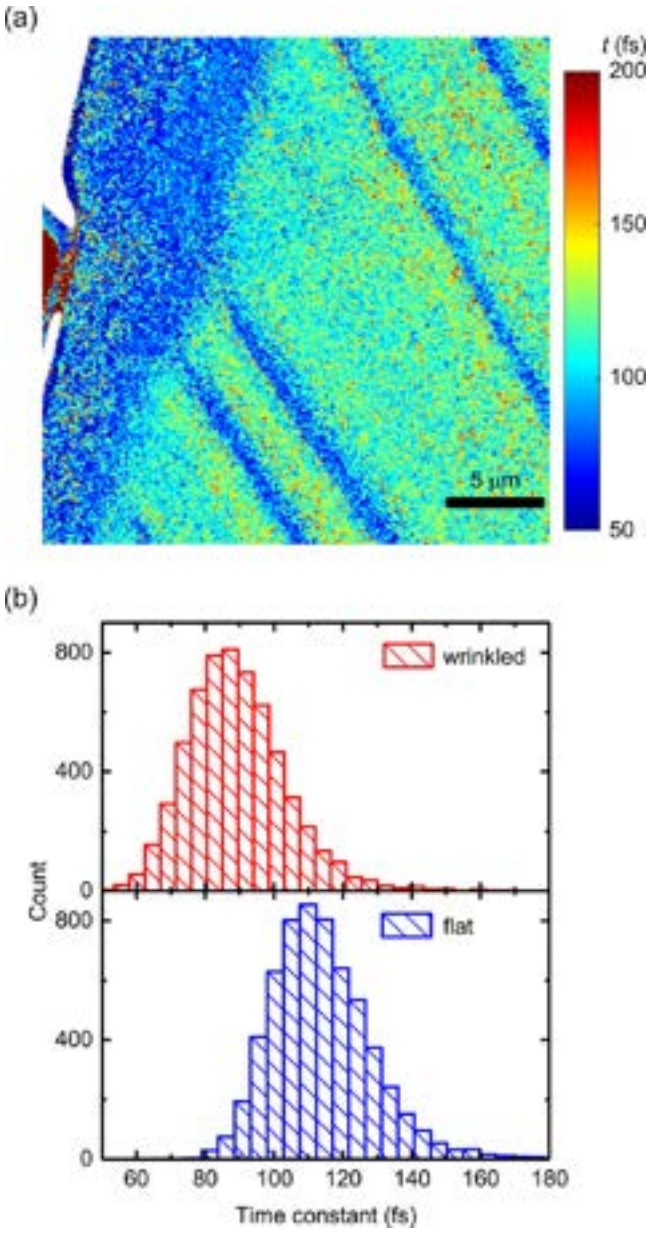

Figure 5. (a) Lifetime map of electronic relaxation. (b) Histograms of time constants of wrinkled and flat regions shown in Figure 4b.

constructed by mapping the flat system into a wave along the armchair direction with a 25 Å radius of curvature (Figure 6b), as required to maintain the wave shape. The supercell length of the wrinkled system is reduced to 52 Å due to the mapping, and the thickness is increased by 11% to 6.7 Å for each layer, after geometric optimization. The wavelike structure is needed to maintain system periodicity and eliminate artificial electronic states associated with edges. Due to the limited system size (120 atoms per simulation cell), a small 2.5 nm curvature radius is required to maintain the wave shape during thermalization. The e−ph relaxation in the two systems is studied using a combination of real-time time-dependent density functional theory and nonadiabatic (NA) molecular dynamics,[84] as implemented within the PYXAID software (see Supporting Information for details).[85,86]

Bending B-MoS_2 away from its equilibrium geometry to produce wrinkles perturbs interatomic interactions and decreases the width of the electronic bands. We observe a steeper rise of the density of states (DOS) near the CB edge and a reduction of the energy range from the CB edge to the energy where its DOS peak (Figure 6c). Depending on its extent, structural deformation can lead to major changes in the electronic properties, such as a semiconductor-to-metal transition.[50] Here, the DOS changes are ∼10%, sufficient to influence the relaxation dynamics. As the PEEM measurements are not energy resolved, these cannot determine spectral shifts associated with the theoretically predicted shift in the CB DOS. To provide an additional test of the model used, we calculate the electronic properties of a system with a 50% longer simulation cell for flat B-MoS_2 and a twice smaller curvature for curved B-MoS_2 (Figure S7). We observe the same behavior: the curved system has a steeper rising DOS near the CB edge. A denser manifold of electronic states, i.e., higher DOS, results in stronger NA coupling, hence faster e−ph relaxation,[85,86] indicating a faster nonradiative decay in curved B-MoS_2 for excitation energies up to 1 eV above the CB edge.

The simulated electronic relaxation dynamics of flat and curved B-MoS_2, both with an initial excess energy of 1 eV, similar to the experiments, are shown in Figure 6d. Electronic relaxation is faster for curved than flat B-MoS_2, in agreement with experiments (Figure 4c). The simulated quantum dynamics exhibits a short, <100 fs, Gaussian regime, before switching to an exponential decay, as observed experimentally in Figure 4c. The transition to exponential decay occurs after 10 or more states of the Hilbert space. For <100 fs, <10 states are involved in the electronic relaxation, and the Gaussian regime can be regarded as the beginning of a Rabi oscillation.[87] The flat initial part of the decay curve is needed to achieve the quantum Zeno effect, in which a frequent measurement on a quantum system stops the dynamics.[87,88]

Exponential fitting of the simulated dynamics in Figure 6d gives time constants of ∼117 and 90 fs for flat and curved B-MoS_2, respectively, with ∼23% faster electronic relaxation in the curved system. The time constants for different initial excess energies (Figure 6e) show a similar faster relaxation for curved than flat B-MoS_2. The scatter in the low-energy region (∼0−0.3 eV) of Figure 6e is due to the low DOS near the CB edge. There, the dynamics is complex and cannot be simply described by an exponential function, resulting in pronounced fluctuations of the fitted time scale. In the ∼0.3−1.5 eV region, the curved B-MoS_2 shows consistently faster dynamics than the flat one. Overall, a relaxation time constant reduction of ∼10−40% is observed due to wrinkling, consistent with the experimentally observed ∼20% reduction. The difference decreases as the initial energy approaches ∼1.5 eV above the band edge, since the DOS decreases faster in the region for curved B-MoS_2 (Figure 6c). The calculated <100 fs relaxation times for curved MoS_2 over the initial energy range $E - E_{CBM}$ ∼ 0.6−1.5 eV remain shorter than the shortest relaxation time calculated for flat MoS_2 (106 fs, at an initial excess energy of ∼1.3 eV). Hence, the observed faster relaxation dynamics is robust, with respect to changes in the initial excess energy induced by wrinkling.

To provide further insights into the origin of the accelerated electronic relaxation due to wrinkling, we analyze the NA coupling matrix elements, given by[85]

https://doi.org/10.1021/acsnano.3c02917
ACS Nano 2023, 17, 16682−16694

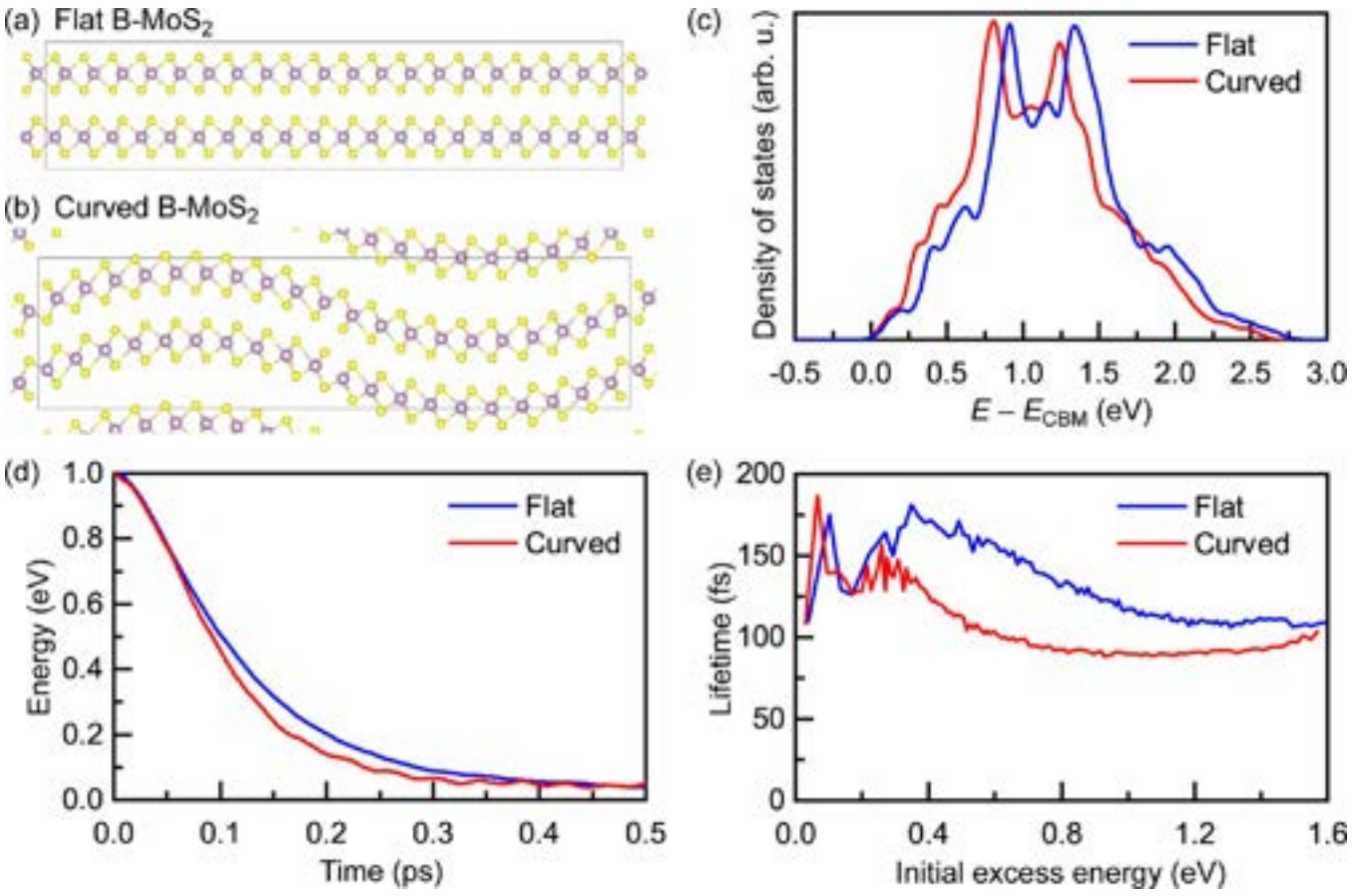

Figure 6. Side views of (a) flat and (b) curved B-MoS_2. The box shows the supercell boundary. (c) CB electronic density of states (DOS). The DOS of the curved system rises more steeply, because the disruption of some interatomic interactions leads to a narrower CB. (d) Electronic relaxation in flat (blue) and curved (red) systems for an initial energy of 1 eV above the CB edge. The fitted time constants are 117 and 90 fs for flat and curved B-MoS_2, respectively. (e) Energy decay time scales for different initial energies above the CB edge. Note that the zero of energy is set to the CB edge in (d, e), while it is inside the bandgap in (c) in order to show the offset of CB edges between flat and curved systems.

$$d_{ij} = -i\hbar\left\langle \Phi_i \middle| \frac{\partial}{\partial t} \middle| \Phi_j \right\rangle = -i\hbar\langle \Phi_i|\nabla_{\mathbf{R}}|\Phi_j\rangle\dot{\mathbf{R}} = -\frac{i\hbar\langle \Phi_i|\nabla_{\mathbf{R}}H|\Phi_j\rangle}{E_j - E_i}\dot{\mathbf{R}} \quad (2)$$

where $\langle \Phi_i|\nabla_{\mathbf{R}}|\Phi_j\rangle$ is the derivative coupling and $\dot{\mathbf{R}}$ is the atomic velocity. The NA coupling between pairs of orbitals Φ_i and Φ_j, starting from the lowest unoccupied molecular orbital (LUMO) up to LUMO+120, for flat and curved B-MoS_2 is shown in Figure 7a and 7b, respectively. The 1 eV excess energy produced by photoexcitation in the experiment would populate the LUMO+65 and LUMO+82 for flat and curved B-MoS_2, respectively. The LUMO+120 resides 1.7 and 1.6 eV above the CB edges of flat and curved B-MoS_2, respectively, with the smaller energy range spanned by 120 orbitals of curved B-MoS_2 reflecting the electronic band narrowing. The NA coupling between adjacent orbitals is larger than that between other terms, evident from the red diagonal strips in Figure 7a,b. However, the red strip covers a broader energy range in the curved system. For pairs of orbitals that reside in the 0−0.7 eV energy range, corresponding to orbitals that span the LUMO to LUMO+40, the NA coupling values are <50 meV in flat and >50 meV in curved B-MoS_2. The larger NA coupling of curved B-MoS_2 accelerates electronic relaxation.

According to eq 2, the NA coupling matrix element d_{ij} is determined by the derivative coupling $\langle \Phi_i|\nabla_{\mathbf{R}}|\Phi_j\rangle$ and the atomic velocity $\dot{R}$. The latter is dependent on the temperature of the system and the atomic mass, both of which are identical for flat and curved B-MoS_2. The difference in the NA couplings for flat and wrinkled B-MoS_2 therefore arises from the $\langle \Phi_i|\nabla_{\mathbf{R}}|\Phi_j\rangle$ term, which encodes the response of the electronic subsystem to atomic motions. Generally, larger amplitude motions give stronger NA coupling, because they lead to larger changes in the wave functions. Figure 7c shows the out-of-plane fluctuations of B-MoS_2 along the nonadiabatic *ab initio* molecular dynamics (NAMD) trajectory. These motions, characterized by the largest amplitude and length scale, are most distinctive between flat and curved B-MoS_2. Local modes, such as Mo−S stretching and S−Mo−S bending, have little dependence on the B-MoS_2 curvature. Curved B-MoS_2 has a ∼2−3× larger out-of-plane oscillation amplitude than flat B-MoS_2, which in turn yields a stronger NA coupling, hence a faster electronic relaxation. For a given strain, an increase in thickness leads to a decrease in the amplitude of out-of-plane motion, which in turn decreases the nonadiabatic coupling, hence slowing electronic relaxation. Figure 7d shows the calculated fast Fourier transform (FFT) power spectra of the phonon modes that mediate electronic relaxation in both flat and curved B-MoS_2. The FFT powers are larger for curved B-

https://doi.org/10.1021/acsnano.3c02917
ACS Nano 2023, 17, 16682−16694

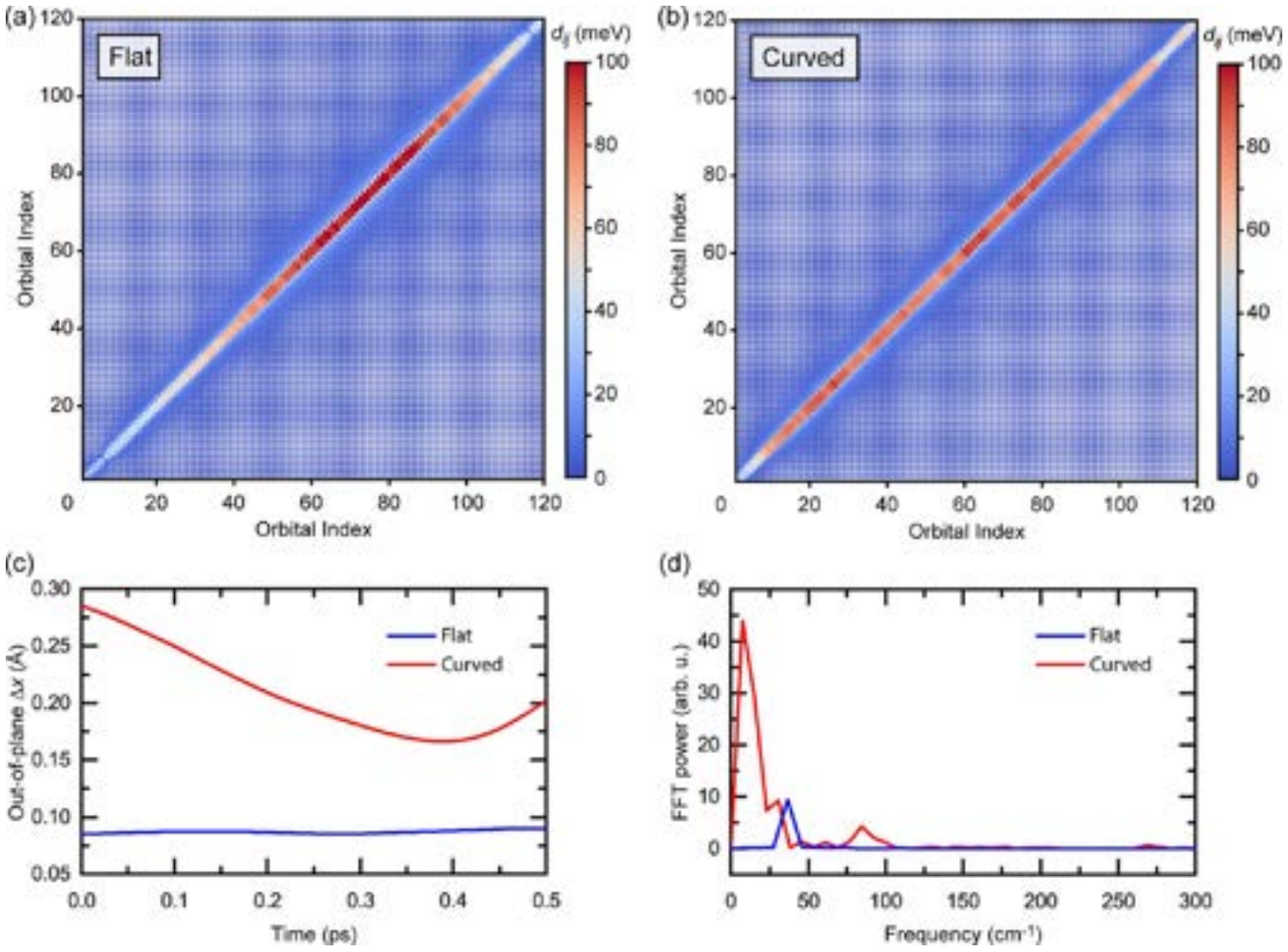

Figure 7. Canonically averaged NA coupling between Kohn−Sham (KS) orbitals in (a) flat and (b) curved B-MoS_2. (c) Average out-of-plane displacement of atoms in flat (blue) and curved (red) B-MoS_2 along the MD trajectories. (d) Calculated FFT power spectra of the phonon modes that mediate electronic relaxation in flat and curved B-MoS_2.

MoS_2, consistent with stronger nonadiabatic coupling and hence faster relaxation dynamics for curved B-MoS_2. The calculated low-frequency peak ~8 cm^{-1} for curved B-MoS_2 is consistent with the previously observed Pos($LBM_{17,16}$) ~ 5.2 cm^{-1} for 17L-MoS_2,[70] whereas the peak ~33 cm^{-1} for flat B-MoS_2 matches the experimentally observed Pos($C_{17,1}$) ~ 34 cm^{-1} in 17L-MoS_2 in Figure 2c and ref 70.

CONCLUSIONS

We used the high spatial and temporal resolution of TR-PEEM to investigate the spatially heterogeneous ultrafast dynamics of wrinkled ML-MoS_2. Probing the ultrafast dynamics at the Γ point reveals faster electronic relaxation for wrinkled regions than for flat regions. Nonadiabatic *ab initio* molecular dynamics shows that electron−phonon coupling is enhanced by wrinkling, hence facilitating electronic relaxation. Our study suggests that the sub-picosecond electronic relaxation dynamics of TMDs is amenable to strain engineering and that applications that require long-lived hot carriers, such as hot-e-driven light harvesting[89] and photocatalysis,[90] should employ wrinkle-free TMDs.

METHODS

Sample Preparation. Wrinkled ML-MoS_2 is prepared as follows. A 2H-MoS_2 bulk crystal grown by chemical vapor transport[91] is exfoliated by micromechanical cleavage (MC) on Nitto Denko tape[92] and then placed onto a polydimethylsiloxane (PDMS) stamp[93] (~1 × 1 cm^2) attached to a glass slide for inspection under an optical microscope. Optical contrast is used to estimate the flake thickness prior to transfer.[94] The PMDS stamp with the selected ML-MoS_2 flake is then cut with a razor blade to a smaller size (~1.5 × 1.5 mm^2). The glass slide with the ML-MoS_2/PMDS stamp is fixed by vacuum on a positioner with motorized *xyz* micromanipulators under an optical microscope. It is then tilted by ~10−15° with respect to the target substrate. The larger the tilt angle,[93] the stronger the pressure applied by the *z* micromanipulator to deform the PDMS upon coming in contact with the target substrate, and the greater the strain induced during transfer.[93,95] Thus, the pressure is varied with tilt angle and PDMS size. Prepatterned Au/Cr (50/2 nm) pads of 2 × 2 mm^2 are defined by a shadow mask, using Kapton tape on 90 nm SiO_2/Si, followed by thermal evaporation at ~5 × 10^{-7} Torr at 0.5 Å/s. Before transfer, the Au surface is cleaned in acetone and isopropanol for 30 s each, followed by 60 s plasma treatment at 10 W.[96] ML-MoS_2/PDMS flakes are then aligned on the Au pads at 40 °C and stamped using motorized *xyz* micromanipulators. After ML-MoS_2 touches the Au substrate, the temperature is increased to 60 °C. This results in different thermal expansion for PDMS,[97] ML-MoS_2,[98] and Au,[99] inducing the formation of wrinkles. At 60 °C, PDMS is peeled off with the motorized *xyz* micromanipulators, leaving wrinkled ML-MoS_2 on

https://doi.org/10.1021/acsnano.3c02917
ACS Nano 2023, 17, 16682−16694

Au. All wrinkles are formed due to the same process, i.e., a combination of thermal expansion mismatch and deformation of the PDMS stamp, and, as such, most likely belong to the same type.

Sample Characterization. AFM images are acquired with a Bruker Dimension Icon in tapping mode. Raman measurements are taken with a Horiba LabRam HR Evolution confocal system, equipped with a 1800 l/mm grating, volume Bragg filters with a cutoff frequency of ~5 cm^{-1} at 514 nm, and a 100× objective (numerical aperture = 0.9), resulting in a spot size of ~1 μm. The laser power is kept at <0.1 mW to avoid sample damage. Identification of N for $N > 5$ requires measurements of Pos(C) with a precision that exceeds the spectral resolution of the system (typical shift of ~0.1 cm^{-1} vs spectral resolution of ~0.6 cm^{-1}). However, peak position evaluation with subpixel accuracy can be achieved via spectral fitting.[73] The accuracy is determined by fitting error, statistical errors arising from spatial variation, CCD noise, and errors associated with the registry of pixels relative to the position of peaks.[73] The latter provides the largest contribution to the total error, limiting the accuracy to ±0.06 cm^{-1}.[73]

TR-PEEM Measurements. We use a high-repetition-rate, high-power Yb fiber laser (Tangerine 30, Amplitude Systemes), which delivers 40 μJ, 320 fs pulses at 0.6 MHz and a 1.03 μm center wavelength (1.20 eV photon energy). After spectral broadening in a Xe-filled hollow-core fiber,[100] a combination of highly dispersive chirped mirrors and a pair of wedges compress pulses to 50 fs FHWM duration. Second and third harmonics, with photon energies of ~2.41 and 3.61 eV, are generated through nonlinear frequency conversion steps in β-barium borate crystals, followed by temporal compression using a prism pair. The FWHM pulse duration of the second harmonic, which acts as a pump beam, is ~46 fs, whereas that of the third harmonic, acting as a probe, is ~40 fs. The pump beam is sent into a computer-controlled optical delay line to vary the time delay between pump and probe pulses. The overall time resolution, as determined by pump−probe cross-correlation at the sample position, is ~55 fs FWHM. The error bars reported for the decay time constants correspond to the standard error of the fit. The PEEM microscope (Focus GmbH, PEEM-IS) has a spatial resolution of ~77 nm according to the 16−84% criterion, defined as the distance over which the image intensity decreases from 84% to 16% of its maximum.[67,101] At each time delay, the image acquisition time is 19 s.

Theoretical Simulations. The geometric structure optimization and adiabatic molecular dynamics (MD) simulations are performed with the Vienna Ab initio Simulation Package (VASP),[102−104] employing the Perdew−Burke−Ernzerhof (PBE) exchange−correlation functional[105] and the projector augmented wave (PAW) method.[106] The van der Waals interactions are treated using the DFT-D3 method,[107,108] as they are critical for LMs. The Brillouin zone is sampled with 7 × 1 × 3 Γ-centered Monkhorst−Pack grids,[109] and the energy cutoff for the plane wave basis is set to 340 eV. After geometry optimization, we perform adiabatic MD. First, we heat the systems to 300 K with the Nose-Hoover thermostat[110,111] and thermalize for 2 ps. Then, we generate 2 ps microcanonical trajectories with a 1 fs time step. Using the generated trajectories, we perform NAMD simulations implemented within the real-time time-dependent density functional theory framework[84] in PYXAID.[85,86] Phase correction and state ordering are incorporated before computing NA coupling.[112,113] Fewest switches surface hopping[114] (FSSH) is used to study hot e relaxation. To mimic the experiments, we performed multiple NAMD simulations on each system with different initial excitations. These start with electrons residing in Kohn−Sham orbitals within the CB with energies from 0 to ~1.5 eV relative to the CB edge. We perform 1000 stochastic FSSH realizations for each initial configuration.

ASSOCIATED CONTENT

Supporting Information

The Supporting Information is available free of charge at https://pubs.acs.org/doi/10.1021/acsnano.3c02917.

AFM measurements, static PEEM image and calculated density of states, determination of photon order and probe window, extended time traces of wrinkled and flat 17L-MoS_2, electronic structure of a larger wrinkled B-MoS_2 (PDF)

AUTHOR INFORMATION

Corresponding Authors

Andrea C. Ferrari − *Cambridge Graphene Centre, University of Cambridge, Cambridge CB3 0FA, United Kingdom*; Email: acf26@cam.ac.uk

Oleg V. Prezhdo − *Department of Physics and Astronomy and Department of Chemistry, University of Southern California, Los Angeles, California 90089, United States*; orcid.org/0000-0002-5140-7500; Email: prezhdo@usc.edu

Zhi-Heng Loh − *School of Chemistry, Chemical Engineering and Biotechnology, and School of Physical and Mathematical Sciences, Nanyang Technological University, Singapore 637371, Singapore*; orcid.org/0000-0001-9729-9632; Email: zhiheng@ntu.edu.sg

Authors

Ce Xu − *School of Chemistry, Chemical Engineering and Biotechnology, and School of Physical and Mathematical Sciences, Nanyang Technological University, Singapore 637371, Singapore*

Guoqing Zhou − *Department of Physics and Astronomy, University of Southern California, Los Angeles, California 90089, United States*; orcid.org/0000-0002-4000-8467

Evgeny M. Alexeev − *Cambridge Graphene Centre, University of Cambridge, Cambridge CB3 0FA, United Kingdom*; orcid.org/0000-0002-8149-6364

Alisson R. Cadore − *Cambridge Graphene Centre, University of Cambridge, Cambridge CB3 0FA, United Kingdom*

Ioannis Paradisanos − *Cambridge Graphene Centre, University of Cambridge, Cambridge CB3 0FA, United Kingdom*; orcid.org/0000-0001-8310-710X

Anna K. Ott − *Cambridge Graphene Centre, University of Cambridge, Cambridge CB3 0FA, United Kingdom*

Giancarlo Soavi − *Cambridge Graphene Centre, University of Cambridge, Cambridge CB3 0FA, United Kingdom*; orcid.org/0000-0003-2434-2251

Sefaattin Tongay − *School for Engineering of Matter, Transport and Energy, Arizona State University, Tempe, Arizona 85287, United States*; orcid.org/0000-0001-8294-984X

Giulio Cerullo − *Department of Physics, Politecnico di Milano, I-20133 Milano, Italy; IFN-CNR, I-20133 Milano, Italy*; orcid.org/0000-0002-9534-2702

Complete contact information is available at: https://pubs.acs.org/10.1021/acsnano.3c02917

Notes

The authors declare no competing financial interest.

ACKNOWLEDGMENTS

We acknowledge funding from the Ministry of Education, Singapore (MOE-T2EP50221-0004 and RG1/22), the EU Graphene Flagship, ERC Grants Hetero2D, GIPT, EU Grants GRAP-X, CHARM, EPSRC Grants EP/K01711X/1, EP/K017144/1, EP/N010345/1, EP/L016087/1, EP/V000055/

1, and EP/X015742/1, and the U.S. National Science Foundation (CHE-2154367).

REFERENCES

(1) Wang, Q. H.; Kalantar-Zadeh, K.; Kis, A.; Coleman, J. N.; Strano, M. S. Electronics and Optoelectronics of Two-Dimensional Transition Metal Dichalcogenides. *Nat. Nanotechnol.* **2012**, *7* (11), 699−712.

(2) Ferrari, A. C.; Bonaccorso, F.; Fal'ko, V.; Novoselov, K. S.; Roche, S.; Bøggild, P.; Borini, S.; Koppens, F. H. L.; Palermo, V.; Pugno, N.; Garrido, J. A.; Sordan, R.; Bianco, A.; Ballerini, L.; Prato, M.; Lidorikis, E.; Kivioja, J.; Marinelli, C.; Ryhänen, T.; Morpurgo, A.; et al. Science and Technology Roadmap for Graphene, Related Two-Dimensional Crystals, and Hybrid Systems. *Nanoscale* **2015**, *7* (11), 4598−4810.

(3) Choi, W.; Choudhary, N.; Han, G. H.; Park, J.; Akinwande, D.; Lee, Y. H. Recent Development of Two-Dimensional Transition Metal Dichalcogenides and Their Applications. *Mater. Today* **2017**, *20* (3), 116−130.

(4) Bonaccorso, F.; Lombardo, A.; Hasan, T.; Sun, Z.; Colombo, L.; Ferrari, A. C. Production and Processing of Graphene and 2d Crystals. *Mater. Today* **2012**, *15* (12), 564−589.

(5) Backes, C.; Abdelkader, A. M.; Alonso, C.; Andrieux-Ledier, A.; Arenal, R.; Azpeitia, J.; Balakrishnan, N.; Banszerus, L.; Barjon, J.; Bartali, R.; Bellani, S.; Berger, C.; Berger, R.; Ortega, M. M. B.; Bernard, C.; Beton, P. H.; Beyer, A.; Bianco, A.; Bøggild, P.; Bonaccorso, F.; et al. Production and Processing of Graphene and Related Materials. *2D Mater.* **2020**, *7* (2), No. 022001.

(6) Mak, K. F.; Lee, C.; Hone, J.; Shan, J.; Heinz, T. F. Atomically Thin MoS_2: A New Direct-Gap Semiconductor. *Phys. Rev. Lett.* **2010**, *105* (13), No. 136805.

(7) Splendiani, A.; Sun, L.; Zhang, Y.; Li, T.; Kim, J.; Chim, C.-Y.; Galli, G.; Wang, F. Emerging Photoluminescence in Monolayer MoS_2. *Nano Lett.* **2010**, *10* (4), 1271−1275.

(8) Radisavljevic, B.; Kis, A. Mobility Engineering and a Metal−Insulator Transition in Monolayer MoS_2. *Nat. Mater.* **2013**, *12* (9), 815−820.

(9) Kang, K.; Xie, S.; Huang, L.; Han, Y.; Huang, P. Y.; Mak, K. F.; Kim, C.-J.; Muller, D.; Park, J. High-Mobility Three-Atom-Thick Semiconducting Films with Wafer-Scale Homogeneity. *Nature* **2015**, *520* (7549), 656−660.

(10) Mak, K. F.; He, K.; Shan, J.; Heinz, T. F. Control of Valley Polarization in Monolayer MoS_2 by Optical Helicity. *Nat. Nanotechnol.* **2012**, *7* (8), 494−498.

(11) Wang, Z.; Molina-Sánchez, A.; Altmann, P.; Sangalli, D.; De Fazio, D.; Soavi, G.; Sassi, U.; Bottegoni, F.; Ciccacci, F.; Finazzi, M.; Wirtz, L.; Ferrari, A. C.; Marini, A.; Cerullo, G.; Dal Conte, S. Intravalley Spin−Flip Relaxation Dynamics in Single-Layer WS_2. *Nano Lett.* **2018**, *18* (11), 6882−6891.

(12) Bikorimana, S.; Lama, P.; Walser, A.; Dorsinville, R.; Anghel, S.; Mitioglu, A.; Micu, A.; Kulyuk, L. Nonlinear Optical Responses in Two-Dimensional Transition Metal Dichalcogenide Multilayer: WS_2, WSe_2, MoS_2 and $Mo_{0.5}w_{0.5}s_2$. *Opt. Express* **2016**, *24* (18), 20685−20695.

(13) Säynätjoki, A.; Karvonen, L.; Rostami, H.; Autere, A.; Mehravar, S.; Lombardo, A.; Norwood, R. A.; Hasan, T.; Peyghambarian, N.; Lipsanen, H.; Kieu, K.; Ferrari, A. C.; Polini, M.; Sun, Z. Ultra-Strong Nonlinear Optical Processes and Trigonal Warping in MoS_2 Layers. *Nat. Commun.* **2017**, *8* (1), 893.

(14) Lafeta, L.; Corradi, A.; Zhang, T.; Kahn, E.; Bilgin, I.; Carvalho, B. R.; Kar, S.; Terrones, M.; Malard, L. M. Second- and Third-Order Optical Susceptibilities across Excitons States in 2D Monolayer Transition Metal Dichalcogenides. *2D Mater.* **2021**, *8* (3), No. 035010.

(15) Chernikov, A.; Berkelbach, T. C.; Hill, H. M.; Rigosi, A.; Li, Y.; Aslan, O. B.; Reichman, D. R.; Hybertsen, M. S.; Heinz, T. F. Exciton Binding Energy and Nonhydrogenic Rydberg Series in Monolayer WS_2. *Phys. Rev. Lett.* **2014**, *113* (7), No. 076802.

(16) Bellus, M. Z.; Ceballos, F.; Chiu, H.-Y.; Zhao, H. Tightly Bound Trions in Transition Metal Dichalcogenide Heterostructures. *ACS Nano* **2015**, *9* (6), 6459−6464.

(17) Scarpelli, L.; Masia, F.; Alexeev, E. M.; Withers, F.; Tartakovskii, A. I.; Novoselov, K. S.; Langbein, W. Resonantly Excited Exciton Dynamics in Two-Dimensional $MoSe_2$ Monolayers. *Phys. Rev. B* **2017**, *96* (4), No. 045407.

(18) Paradisanos, I.; Wang, G.; Alexeev, E. M.; Cadore, A. R.; Marie, X.; Ferrari, A. C.; Glazov, M. M.; Urbaszek, B. Efficient Phonon Cascades in WSe_2 Monolayers. *Nat. Commun.* **2021**, *12* (1), 538.

(19) Bonaccorso, F.; Sun, Z.; Hasan, T.; Ferrari, A. C. Graphene Photonics and Optoelectronics. *Nat. Photonics* **2010**, *4* (9), 611−622.

(20) Koppens, F.; Mueller, T.; Avouris, P.; Ferrari, A.; Vitiello, M.; Polini, M. Photodetectors Based on Graphene, Other Two-Dimensional Materials and Hybrid Systems. *Nat. Nanotechnol.* **2014**, *9* (10), 780.

(21) Gadelha, A. C.; Cadore, A. R.; Watanabe, K.; Taniguchi, T.; de Paula, A. M.; Malard, L. M.; Lacerda, R. G.; Campos, L. C. Gate-Tunable Non-Volatile Photomemory Effect in MoS_2 Transistors. *2D Mater.* **2019**, *6* (2), No. 025036.

(22) Orchin, G. J.; De Fazio, D.; Di Bernardo, A.; Hamer, M.; Yoon, D.; Cadore, A. R.; Goykhman, I.; Watanabe, K.; Taniguchi, T.; Robinson, J. W. Niobium Diselenide Superconducting Photodetectors. *Appl. Phys. Lett.* **2019**, *114* (25), No. 251103.

(23) Sundaram, R.; Engel, M.; Lombardo, A.; Krupke, R.; Ferrari, A.; Avouris, P.; Steiner, M. Electroluminescence in Single Layer MoS_2. *Nano Lett.* **2013**, *13* (4), 1416−1421.

(24) Palacios-Berraquero, C.; Barbone, M.; Kara, D. M.; Chen, X.; Goykhman, I.; Yoon, D.; Ott, A. K.; Beitner, J.; Watanabe, K.; Taniguchi, T.; Ferrari, A. C.; Atatüre, M. Atomically Thin Quantum Light-Emitting Diodes. *Nat. Commun.* **2016**, *7* (1), 12978.

(25) Wang, J.; Verzhbitskiy, I.; Eda, G. Electroluminescent Devices Based on 2D Semiconducting Transition Metal Dichalcogenides. *Adv. Mater.* **2018**, *30* (47), No. 1802687.

(26) Sun, Z.; Martinez, A.; Wang, F. Optical Modulators with 2D Layered Materials. *Nat. Photonics* **2016**, *10* (4), 227.

(27) Wang, H. T.; Yuan, H. T.; Hong, S. S.; Li, Y. B.; Cui, Y. Physical and Chemical Tuning of Two-Dimensional Transition Metal Dichalcogenides. *Chem. Soc. Rev.* **2015**, *44* (9), 2664−2680.

(28) Zhou, J.; Lin, J.; Huang, X.; Zhou, Y.; Chen, Y.; Xia, J.; Wang, H.; Xie, Y.; Yu, H.; Lei, J.; Wu, D.; Liu, F.; Fu, Q.; Zeng, Q.; Hsu, C.-H.; Yang, C.; Lu, L.; Yu, T.; Shen, Z.; Lin, H.; et al. A Library of Atomically Thin Metal Chalcogenides. *Nature* **2018**, *556* (7701), 355−359.

(29) Friend, R. H.; Yoffe, A. D. Electronic Properties of Intercalation Complexes of Transition-Metal Dichalcogenides. *Adv. Phys.* **1987**, *36* (1), 1−94.

(30) Tedstone, A. A.; Lewis, D. J.; O'Brien, P. Synthesis, Properties, and Applications of Transition Metal-Doped Layered Transition Metal Dichalcogenides. *Chem. Mater.* **2016**, *28* (7), 1965−1974.

(31) Chen, Y. F.; Xi, J. Y.; Dumcenco, D. O.; Liu, Z.; Suenaga, K.; Wang, D.; Shuai, Z. G.; Huang, Y. S.; Xie, L. M. Tunable Band Gap Photoluminescence from Atomically Thin Transition-Metal Dichalcogenide Alloys. *ACS Nano* **2013**, *7* (5), 4610−4616.

(32) Xie, L. M. Two-Dimensional Transition Metal Dichalcogenide Alloys: Preparation, Characterization and Applications. *Nanoscale* **2015**, *7* (44), 18392−18401.

(33) Ramasubramaniam, A.; Naveh, D.; Towe, E. Tunable Band Gaps in Bilayer Transition-Metal Dichalcogenides. *Phys. Rev. B* **2011**, *84* (20), No. 205325.

(34) Klein, J.; Wierzbowski, J.; Regler, A.; Becker, J.; Heimbach, F.; Muller, K.; Kaniber, M.; Finley, J. J. Stark Effect Spectroscopy of Mono- and Few-Layer MoS_2. *Nano Lett.* **2016**, *16* (3), 1554−1559.

(35) Nayak, A. P.; Bhattacharyya, S.; Zhu, J.; Liu, J.; Wu, X.; Pandey, T.; Jin, C.; Singh, A. K.; Akinwande, D.; Lin, J.-F. Pressure-Induced Semiconducting to Metallic Transition in Multilayered Molybdenum Disulphide. *Nat. Commun.* **2014**, *5* (1), 3731.

(36) Garcia, A. M.; del Corro, E.; Kalbac, M.; Frank, O. Tuning the Electronic Properties of Monolayer and Bilayer Transition Metal

https://doi.org/10.1021/acsnano.3c02917
ACS Nano 2023, 17, 16682−16694

Dichalcogenide Compounds under Direct out-of-Plane Compression. *Phys. Chem. Chem. Phys.* **2017**, *19* (20), 13333−13340.
(37) Deng, S. K.; Sumant, A. V.; Berry, V. Strain Engineering in Two-Dimensional Nanomaterials Beyond Graphene. *Nano Today* **2018**, *22*, 14−35.
(38) Sun, Y.; Liu, K. Strain Engineering in Functional 2-Dimensional Materials. *J. Appl. Phys.* **2019**, *125* (8), No. 082402.
(39) Palacios-Berraquero, C.; Kara, D. M.; Montblanch, A. R. P.; Barbone, M.; Latawiec, P.; Yoon, D.; Ott, A. K.; Loncar, M.; Ferrari, A. C.; Atatüre, M. Large-Scale Quantum-Emitter Arrays in Atomically Thin Semiconductors. *Nat. Commun.* **2017**, *8* (1), 15093.
(40) Montblanch, A. R. P.; Kara, D. M.; Paradisanos, I.; Purser, C. M.; Feuer, M. S. G.; Alexeev, E. M.; Stefan, L.; Qin, Y.; Blei, M.; Wang, G.; Cadore, A. R.; Latawiec, P.; Lončar, M.; Tongay, S.; Ferrari, A. C.; Atatüre, M. Confinement of Long-Lived Interlayer Excitons in WS_2/WSe_2 Heterostructures. *Commun. Phys.* **2021**, *4* (1), 119.
(41) Bertolazzi, S.; Brivio, J.; Kis, A. Stretching and Breaking of Ultrathin MoS_2. *ACS Nano* **2011**, *5* (12), 9703−9709.
(42) Castellanos-Gomez, A.; Poot, M.; Steele, G. A.; Van Der Zant, H. S.; Agraït, N.; Rubio-Bollinger, G. Elastic Properties of Freely Suspended MoS_2 Nanosheets. *Adv. Mater.* **2012**, *24* (6), 772−775.
(43) Cooper, R. C.; Lee, C.; Marianetti, C. A.; Wei, X.; Hone, J.; Kysar, J. W. Nonlinear Elastic Behavior of Two-Dimensional Molybdenum Disulfide. *Phys. Rev. B* **2013**, *87* (3), No. 035423.
(44) Chang, H.-Y.; Yang, S.; Lee, J.; Tao, L.; Hwang, W.-S.; Jena, D.; Lu, N.; Akinwande, D. High-Performance, Highly Bendable MoS_2 Transistors with High-K Dielectrics for Flexible Low-Power Systems. *ACS Nano* **2013**, *7* (6), 5446−5452.
(45) Liu, K.; Yan, Q.; Chen, M.; Fan, W.; Sun, Y.; Suh, J.; Fu, D.; Lee, S.; Zhou, J.; Tongay, S.; Ji, J.; Neaton, J. B.; Wu, J. Elastic Properties of Chemical-Vapor-Deposited Monolayer MoS_2, WS_2, and Their Bilayer Heterostructures. *Nano Lett.* **2014**, *14* (9), 5097−5103.
(46) Dai, Z.; Liu, L.; Zhang, Z. Strain Engineering of 2D Materials: Issues and Opportunities at the Interface. *Adv. Mater.* **2019**, *31* (45), No. 1805417.
(47) Carrascoso, F.; Li, H.; Frisenda, R.; Castellanos-Gomez, A. Strain Engineering in Single-, Bi- and Tri-Layer MoS_2, $MoSe_2$, WS_2 and WSe_2. *Nano Res.* **2021**, *14* (6), 1698−1703.
(48) Castellanos-Gomez, A.; Roldán, R.; Cappelluti, E.; Buscema, M.; Guinea, F.; van der Zant, H. S.; Steele, G. A. Local Strain Engineering in Atomically Thin MoS_2. *Nano Lett.* **2013**, *13* (11), 5361−5366.
(49) He, K.; Poole, C.; Mak, K. F.; Shan, J. Experimental Demonstration of Continuous Electronic Structure Tuning Via Strain in Atomically Thin MoS_2. *Nano Lett.* **2013**, *13* (6), 2931−2936.
(50) Bhattacharyya, S.; Pandey, T.; Singh, A. K. Effect of Strain on Electronic and Thermoelectric Properties of Few Layers to Bulk MoS_2. *Nanotechnology* **2014**, *25* (46), No. 465701.
(51) Johari, P.; Shenoy, V. B. Tuning the Electronic Properties of Semiconducting Transition Metal Dichalcogenides by Applying Mechanical Strains. *ACS Nano* **2012**, *6* (6), 5449−5456.
(52) Li, H.; Contryman, A. W.; Qian, X.; Ardakani, S. M.; Gong, Y.; Wang, X.; Weisse, J. M.; Lee, C. H.; Zhao, J.; Ajayan, P. M.; Li, J.; Manoharan, H. C.; Zheng, X. Optoelectronic Crystal of Artificial Atoms in Strain-Textured Molybdenum Disulphide. *Nat. Commun.* **2015**, *6* (1), 7381.
(53) Jain, J. R.; Hryciw, A.; Baer, T. M.; Miller, D. A.; Brongersma, M. L.; Howe, R. T. A Micromachining-Based Technology for Enhancing Germanium Light Emission Via Tensile Strain. *Nat. Photonics* **2012**, *6* (6), 398.
(54) Deng, S. K.; Che, S. W.; Debbarma, R.; Berry, V. Strain in a Single Wrinkle on an MoS_2 Flake for in-Plane Realignment of Band Structure for Enhanced Photo-Response. *Nanoscale* **2019**, *11* (2), 504−511.
(55) Liu, T.; Liu, S.; Tu, K.-H.; Schmidt, H.; Chu, L.; Xiang, D.; Martin, J.; Eda, G.; Ross, C. A.; Garaj, S. Crested Two-Dimensional Transistors. *Nat. Nanotechnol.* **2019**, *14* (3), 223−226.
(56) Shin, B. G.; Han, G. H.; Yun, S. J.; Oh, H. M.; Bae, J. J.; Song, Y. J.; Park, C.-Y.; Lee, Y. H. Indirect Bandgap Puddles in Monolayer MoS_2 by Substrate-Induced Local Strain. *Adv. Mater.* **2016**, *28* (42), 9378−9384.
(57) Roldán, R.; Castellanos-Gomez, A.; Cappelluti, E.; Guinea, F. Strain Engineering in Semiconducting Two-Dimensional Crystals. *J. Phys.: Condens. Matter* **2015**, *27* (31), No. 313201.
(58) Shah, J. *Ultrafast Spectroscopy of Semiconductors and Semiconductor Nanostructures*; Springer, 2013.
(59) Yang, Y.; Fang, W.-H.; Benderskii, A.; Long, R.; Prezhdo, O. V. Strain Controls Charge Carrier Lifetimes in Monolayer WSe_2: Ab Initio Time Domain Analysis. *J. Phys. Chem. Lett.* **2019**, *10* (24), 7732−7739.
(60) Tian, Y.; Zheng, Q.; Zhao, J. Tensile Strain-Controlled Photogenerated Carrier Dynamics at the Van Der Waals Heterostructure Interface. *J. Phys. Chem. Lett.* **2020**, *11* (3), 586−590.
(61) Niehues, I.; Schmidt, R.; Drüppel, M.; Marauhn, P.; Christiansen, D.; Selig, M.; Berghäuser, G.; Wigger, D.; Schneider, R.; Braasch, L.; Koch, R.; Castellanos-Gomez, A.; Kuhn, T.; Knorr, A.; Malic, E.; Rohlfing, M.; Michaelis de Vasconcellos, S.; Bratschitsch, R. Strain Control of Exciton−Phonon Coupling in Atomically Thin Semiconductors. *Nano Lett.* **2018**, *18* (3), 1751−1757.
(62) Dąbrowski, M.; Dai, Y.; Petek, H. Ultrafast Microscopy: Imaging Light with Photoelectrons on the Nano−Femto Scale. *J. Phys. Chem. Lett.* **2017**, *8* (18), 4446−4455.
(63) Dąbrowski, M.; Dai, Y.; Petek, H. Ultrafast Photoemission Electron Microscopy: Imaging Plasmons in Space and Time. *Chem. Rev.* **2020**, *120* (13), 6247−6287.
(64) Fukumoto, K.; Onda, K.; Yamada, Y.; Matsuki, T.; Mukuta, T.; Tanaka, S.-i.; Koshihara, S.-y. Femtosecond Time-Resolved Photoemission Electron Microscopy for Spatiotemporal Imaging of Photogenerated Carrier Dynamics in Semiconductors. *Rev. Sci. Instrum.* **2014**, *85* (8), No. 083705.
(65) Man, M. K. L.; Margiolakis, A.; Deckoff-Jones, S.; Harada, T.; Wong, E. L.; Krishna, M. B. M.; Madéo, J.; Winchester, A.; Lei, S.; Vajtai, R.; Ajayan, P. M.; Dani, K. M. Imaging the Motion of Electrons across Semiconductor Heterojunctions. *Nat. Nanotechnol.* **2017**, *12* (1), 36−40.
(66) Wang, L.; Xu, C.; Li, M. Y.; Li, L. J.; Loh, Z.-H. Unraveling Spatially Heterogeneous Ultrafast Carrier Dynamics of Single-Layer WSe_2 by Femtosecond Time-Resolved Photoemission Electron Microscopy. *Nano Lett.* **2018**, *18* (8), 5172−5178.
(67) Doherty, T. A. S.; Winchester, A. J.; Macpherson, S.; Johnstone, D. N.; Pareek, V.; Tennyson, E. M.; Kosar, S.; Kosasih, F. U.; Anaya, M.; Abdi-Jalebi, M.; Andaji-Garmaroudi, Z.; Wong, E. L.; Madéo, J.; Chiang, Y.-H.; Park, J.-S.; Jung, Y.-K.; Petoukhoff, C. E.; Divitini, G.; Man, M. K. L.; Ducati, C.; et al. Performance-Limiting Nanoscale Trap Clusters at Grain Junctions in Halide Perovskites. *Nature* **2020**, *580* (7803), 360−366.
(68) Xu, C.; Yong, H. W.; He, J.; Long, R.; Cadore, A. R.; Paradisanos, I.; Ott, A. K.; Soavi, G.; Tongay, S.; Cerullo, G.; Ferrari, A. C.; Prezhdo, O. V.; Loh, Z.-H. Weak Distance Dependence of Hot-Electron-Transfer Rates at the Interface between Monolayer MoS_2 and Gold. *ACS Nano* **2021**, *15* (1), 819−828.
(69) Li, Y.; Liu, W.; Wang, Y.; Xue, Z.; Leng, Y.-C.; Hu, A.; Yang, H.; Tan, P.-H.; Liu, Y.; Misawa, H.; Sun, Q.; Gao, Y.; Hu, X.; Gong, Q. Ultrafast Electron Cooling and Decay in Monolayer WS_2 Revealed by Time- and Energy-Resolved Photoemission Electron Microscopy. *Nano Lett.* **2020**, *20* (5), 3747−3753.
(70) Zhang, X.; Han, W. P.; Wu, J. B.; Milana, S.; Lu, Y.; Li, Q. Q.; Ferrari, A. C.; Tan, P. H. Raman Spectroscopy of Shear and Layer Breathing Modes in Multilayer MoS_2. *Phys. Rev. B* **2013**, *87* (11), No. 115413.
(71) Pizzi, G.; Milana, S.; Ferrari, A. C.; Marzari, N.; Gibertini, M. Shear and Breathing Modes of Layered Materials. *ACS Nano* **2021**, *15* (8), 12509−12534.
(72) Tan, P. H.; Han, W. P.; Zhao, W. J.; Wu, Z. H.; Chang, K.; Wang, H.; Wang, Y. F.; Bonini, N.; Marzari, N.; Pugno, N.; Savini, G.;

https://doi.org/10.1021/acsnano.3c02917
ACS Nano 2023, 17, 16682−16694

Lombardo, A.; Ferrari, A. C. The Shear Mode of Multilayer Graphene. *Nat. Mater.* **2012**, *11* (4), 294−300.
(73) Chiodini, S.; Kerfoot, J.; Venturi, G.; Mignuzzi, S.; Alexeev, E. M.; Teixeira Rosa, B.; Tongay, S.; Taniguchi, T.; Watanabe, K.; Ferrari, A. C.; Ambrosio, A. Moiré Modulation of Van Der Waals Potential in Twisted Hexagonal Boron Nitride. *ACS Nano* **2022**, *16* (5), 7589−7604.
(74) Li, H.; Zhang, Q.; Yap, C. C. R.; Tay, B. K.; Edwin, T. H. T.; Olivier, A.; Baillargeat, D. From Bulk to Monolayer MoS_2: Evolution of Raman Scattering. *Adv. Funct. Mater.* **2012**, *22* (7), 1385−1390.
(75) Conley, H. J.; Wang, B.; Ziegler, J. I.; Haglund, R. F., Jr.; Pantelides, S. T.; Bolotin, K. I. Bandgap Engineering of Strained Monolayer and Bilayer MoS_2. *Nano Lett.* **2013**, *13* (8), 3626−3630.
(76) Li, Z.; Lv, Y.; Ren, L.; Li, J.; Kong, L.; Zeng, Y.; Tao, Q.; Wu, R.; Ma, H.; Zhao, B.; Wang, D.; Dang, W.; Chen, K.; Liao, L.; Duan, X.; Duan, X.; Liu, Y. Efficient Strain Modulation of 2D Materials Via Polymer Encapsulation. *Nat. Commun.* **2020**, *11* (1), 1151.
(77) Sohier, T.; Ponomarev, E.; Gibertini, M.; Berger, H.; Marzari, N.; Ubrig, N.; Morpurgo, A. F. Enhanced Electron-Phonon Interaction in Multivalley Materials. *Phys. Rev. X* **2019**, *9* (3), No. 031019.
(78) Hüfner, S. *Photoelectron Spectroscopy: Principles and Applications*; Springer, 2013.
(79) Molina-Sánchez, A.; Sangalli, D.; Hummer, K.; Marini, A.; Wirtz, L. Effect of Spin-Orbit Interaction on the Optical Spectra of Single-Layer, Double-Layer, and Bulk MoS_2. *Phys. Rev. B* **2013**, *88* (4), No. 045412.
(80) Mai, C.; Barrette, A.; Yu, Y.; Semenov, Y. G.; Kim, K. W.; Cao, L.; Gundogdu, K. Many-Body Effects in Valleytronics: Direct Measurement of Valley Lifetimes in Single-Layer MoS_2. *Nano Lett.* **2014**, *14* (1), 202−206.
(81) Nie, Z.; Long, R.; Teguh, J. S.; Huang, C.-C.; Hewak, D. W.; Yeow, E. K.; Shen, Z.; Prezhdo, O. V.; Loh, Z.-H. Ultrafast Electron and Hole Relaxation Pathways in Few-Layer MoS_2. *J. Phys. Chem. C* **2015**, *119* (35), 20698−20708.
(82) Nie, Z.; Long, R.; Sun, L.; Huang, C.-C.; Zhang, J.; Xiong, Q.; Hewak, D. W.; Shen, Z.; Prezhdo, O. V.; Loh, Z.-H. Ultrafast Carrier Thermalization and Cooling Dynamics in Few-Layer MoS_2. *ACS Nano* **2014**, *8* (10), 10931−10940.
(83) Keyshar, K.; Berg, M.; Zhang, X.; Vajtai, R.; Gupta, G.; Chan, C. K.; Beechem, T. E.; Ajayan, P. M.; Mohite, A. D.; Ohta, T. Experimental Determination of the Ionization Energies of $MoSe_2$, WS_2, and MoS_2 on SiO_2 Using Photoemission Electron Microscopy. *ACS Nano* **2017**, *11* (8), 8223−8230.
(84) Craig, C. F.; Duncan, W. R.; Prezhdo, O. V. Trajectory Surface Hopping in the Time-Dependent Kohn-Sham Approach for Electron-Nuclear Dynamics. *Phys. Rev. Lett.* **2005**, *95* (16), No. 163001.
(85) Akimov, A. V.; Prezhdo, O. V. The PYXAID Program for Non-Adiabatic Molecular Dynamics in Condensed Matter Systems. *J. Chem. Theory Comput.* **2013**, *9* (11), 4959−4972.
(86) Akimov, A. V.; Prezhdo, O. V. Advanced Capabilities of the PYXAID Program: Integration Schemes, Decoherence Effects, Multiexcitonic States, and Field-Matter Interaction. *J. Chem. Theory Comput.* **2014**, *10* (2), 789−804.
(87) Merlin, R. Rabi Oscillations, Floquet States, Fermi's Golden Rule, and All That: Insights from an Exactly Solvable Two-Level Model. *Am. J. Phys.* **2021**, *89* (1), 26−34.
(88) Kilina, S. V.; Neukirch, A. J.; Habenicht, B. F.; Kilin, D. S.; Prezhdo, O. V. Quantum Zeno Effect Rationalizes the Phonon Bottleneck in Semiconductor Quantum Dots. *Phys. Rev. Lett.* **2013**, *110* (18), No. 180404.
(89) Nozik, A. J. Spectroscopy and Hot Electron Relaxation Dynamics in Semiconductor Quantum Wells and Quantum Dots. *Annu. Rev. Phys. Chem.* **2001**, *52* (1), 193−231.
(90) Clavero, C. Plasmon-Induced Hot-Electron Generation at Nanoparticle/Metal-Oxide Interfaces for Photovoltaic and Photocatalytic Devices. *Nat. Photonics* **2014**, *8* (2), 95−103.
(91) Zhang, X.; Lou, F.; Li, C.; Zhang, X.; Jia, N.; Yu, T.; He, J.; Zhang, B.; Xia, H.; Wang, S.; Tao, X. Flux Method Growth of Bulk MoS_2 Single Crystals and Their Application as a Saturable Absorber. *CrystEngComm* **2015**, *17* (21), 4026−4032.
(92) Novoselov, K. S.; Jiang, D.; Schedin, F.; Booth, T. J.; Khotkevich, V. V.; Morozov, S. V.; Geim, A. K. Two-Dimensional Atomic Crystals. *Proc. Natl. Acad. Sci. U.S.A.* **2005**, *102* (30), 10451−10453.
(93) Castellanos-Gomez, A.; Buscema, M.; Molenaar, R.; Singh, V.; Janssen, L.; van der Zant, H. S. J.; Steele, G. A. Deterministic Transfer of Two-Dimensional Materials by All-Dry Viscoelastic Stamping. *2D Mater.* **2014**, *1* (1), No. 011002.
(94) Casiraghi, C.; Hartschuh, A.; Lidorikis, E.; Qian, H.; Harutyunyan, H.; Gokus, T.; Novoselov, K. S.; Ferrari, A. C. Rayleigh Imaging of Graphene and Graphene Layers. *Nano Lett.* **2007**, *7* (9), 2711−2717.
(95) Jain, A.; Bharadwaj, P.; Heeg, S.; Parzefall, M.; Taniguchi, T.; Watanabe, K.; Novotny, L. Minimizing Residues and Strain in 2D Materials Transferred from PDMS. *Nanotechnology* **2018**, *29* (26), No. 265203.
(96) He, J.; Paradisanos, I.; Liu, T.; Cadore, A. R.; Liu, J.; Churaev, M.; Wang, R. N.; Raja, A. S.; Javerzac-Galy, C.; Roelli, P.; Fazio, D. D.; Rosa, B. L. T.; Tongay, S.; Soavi, G.; Ferrari, A. C.; Kippenberg, T. J. Low-Loss Integrated Nanophotonic Circuits with Layered Semiconductor Materials. *Nano Lett.* **2021**, *21* (7), 2709−2718.
(97) Plechinger, G.; Castellanos-Gomez, A.; Buscema, M.; van der Zant, H. S. J.; Steele, G. A.; Kuc, A.; Heine, T.; Schüller, C.; Korn, T. Control of Biaxial Strain in Single-Layer Molybdenite Using Local Thermal Expansion of the Substrate. *2D Mater.* **2015**, *2* (1), No. 015006.
(98) Island, J. O.; Kuc, A.; Diependaal, E. H.; Bratschitsch, R.; van der Zant, H. S. J.; Heine, T.; Castellanos-Gomez, A. Precise and Reversible Band Gap Tuning in Single-Layer $MoSe_2$ by Uniaxial Strain. *Nanoscale* **2016**, *8* (5), 2589−2593.
(99) Frisenda, R.; Drüppel, M.; Schmidt, R.; Michaelis de Vasconcellos, S.; Perez de Lara, D.; Bratschitsch, R.; Rohlfing, M.; Castellanos-Gomez, A. Biaxial Strain Tuning of the Optical Properties of Single-Layer Transition Metal Dichalcogenides. *npj 2D Mater. Appl.* **2017**, *1* (1), 10.
(100) Lo, S.-Z. A.; Wang, L.; Loh, Z.-H. Pulse Propagation in Hollow-Core Fiber at High-Pressure Regime: Application to Compression of Tens of μJ Pulses and Determination of Nonlinear Refractive Index of Xenon at 1.03μm. *Appl. Opt.* **2018**, *57* (16), 4659−4664.
(101) Aeschlimann, M.; Brixner, T.; Fischer, A.; Kramer, C.; Melchior, P.; Pfeiffer, W.; Schneider, C.; Strüber, C.; Tuchscherer, P.; Voronine, D. V. Coherent Two-Dimensional Nanoscopy. *Science* **2011**, *333* (6050), 1723−1726.
(102) Kresse, G.; Hafner, J. Ab Initio Molecular-Dynamics Simulation of the Liquid-Metal−Amorphous-Semiconductor Transition in Germanium. *Phys. Rev. B* **1994**, *49* (20), 14251.
(103) Kresse, G.; Furthmuller, J. Efficient Iterative Schemes for Ab Initio Total-Energy Calculations Using a Plane-Wave Basis Set. *Phys. Rev. B* **1996**, *54* (16), 11169−11186.
(104) Kresse, G.; Furthmuller, J. Efficiency of Ab-Initio Total Energy Calculations for Metals and Semiconductors Using a Plane-Wave Basis Set. *Comput. Mater. Sci.* **1996**, *6* (1), 15−50.
(105) Perdew, J. P.; Burke, K.; Ernzerhof, M. Generalized Gradient Approximation Made Simple. *Phys. Rev. Lett.* **1996**, *77* (18), 3865−3868.
(106) Blochl, P. E. Projector Augmented-Wave Method. *Phys. Rev. B* **1994**, *50* (24), 17953−17979.
(107) Grimme, S.; Antony, J.; Ehrlich, S.; Krieg, H. A Consistent and Accurate Ab Initio Parametrization of Density Functional Dispersion Correction (DFT-D) for the 94 Elements H-Pu. *J. Chem. Phys.* **2010**, *132* (15), No. 154104.
(108) Grimme, S.; Ehrlich, S.; Goerigk, L. Effect of the Damping Function in Dispersion Corrected Density Functional Theory. *J. Comput. Chem.* **2011**, *32* (7), 1456−1465.
(109) Monkhorst, H. J.; Pack, J. D. Special Points for Brillouin-Zone Integrations. *Phys. Rev. B* **1976**, *13* (12), 5188−5192.

https://doi.org/10.1021/acsnano.3c02917
ACS Nano 2023, 17, 16682−16694

(110) Nosé, S. A Unified Formulation of the Constant Temperature Molecular Dynamics Methods. *J. Chem. Phys.* **1984**, *81* (1), 511−519.
(111) Hoover, W. G. Canonical Dynamics: Equilibrium Phase-Space Distributions. *Phys. Rev. A* **1985**, *31* (3), 1695.
(112) Akimov, A. V. A Simple Phase Correction Makes a Big Difference in Nonadiabatic Molecular Dynamics. *J. Phys. Chem. Lett.* **2018**, *9* (20), 6096−6102.
(113) Chu, W.; Zheng, Q.; Akimov, A. V.; Zhao, J.; Saidi, W. A.; Prezhdo, O. V. Accurate Computation of Nonadiabatic Coupling with Projector Augmented-Wave Pseudopotentials. *J. Phys. Chem. Lett.* **2020**, *11* (23), 10073−10080.
(114) Tully, J. C. Molecular Dynamics with Electronic Transitions. *J. Chem. Phys.* **1990**, *93* (2), 1061−1071.

https://doi.org/10.1021/acsnano.3c02917
ACS Nano 2023, 17, 16682−16694